Interplay of intercalation dynamics and lithium plating in monolithic and architectured graphite anodes during fast charging

Aleksandar S. Mijailovic[a,=], Seth Waag-Swift[a,=], Guanyi Wang[b], Bingyao Zhou[b], Mei Luo[c], Wenquan Lu[c], Qingliu Wu[b], and Brian W. Sheldon[a*]

[a]School of Engineering Brown University, Providence RI, USA
[b]Western Michigan University, Kalamazoo, MI, USA
[c]Argonne National Laboratory, Lemont, IL, USA
[=]Authors contributed equally
[*]Corresponding author

S Supplemental Information

S.1 Experimental strategy and sources of error

A custom visualization cell (Fig.2A) was built to capture local intercalation reaction dynamics in a close approximation of the 1D geometry of a commercial monolithic electrode. With our approach, it is possible to capture the effect on intercalation of the anisotropic microstructures that are produced during electrode casting and calendaring. These effects are lost with common modifications used to facilitate imaging, where the transport direction is parallel to the plane of the manufactured electrode sheet. Due to the large amount of data retrieved from each charge/discharge cycle, an entire array of electrode design conditions (e.g. C-rate, mass loading) can be explored in relatively few experiments. However, plating onset cannot be measured with this setup, as the nucleation of lithium plating can occur anywhere in the electrode (typically the anode/separator interface). Therefore, a separate methodology was used, where anodes were cycled in coin cells, frozen, and analyzed with microscopy post-mortem (Fig.2 E). In this procedure, cells were charged to a specific SOC and transport was halted by freezing them immediately in liquid nitrogen. The anodes were then dissected and imaged to determine plating onset on the graphite/separator surface, and the concurrent intercalation profile through the electrode cross section (Fig.2 G).

Both experimental methodologies provided unique limitations and artifacts. Most notably the in situ experiments had the benefit of measuring the entire charge history, but only provided a small observational window and could not detect the onset of plating. By contrast, the ex situ experiments afford time to examine the entire electrode and could detect plating, but each experiment only produced a single snapshot of time (i.e., each cell was charged to a specific SOC prior to ex situ observation), leading to large uncertainty in the exact onset of plating. The ex situ method was also susceptible to the possibility of relaxation of intercalation and transport gradients, despite the flash freezing step. Thus both experimental methods were designed in parallel to account for artifacts and limitations of each method. This complementary experimental design improved confidence in the interpretation of these results due to consistency between methods (for example compare Fig. 5 and 7). Potential sources of error and corresponding interpretation of results is discussed here.

The presence of in-plane heterogeneity presented in the main text is potentially a large source of error in the in situ results due to the small field of view relative to the electrode size. In order to ground truth the SOC profiles derived from the color image data, we compare the image-derived SOC with the lithium inventory expected from the electrochemical data. In Figure S.5, two representative plots are shown, highlighting small discrepancies between the imaged SOC and the mean SOC of the entire electrode. The small steps or shoulders reflect the limitations of our image processing algorithm to

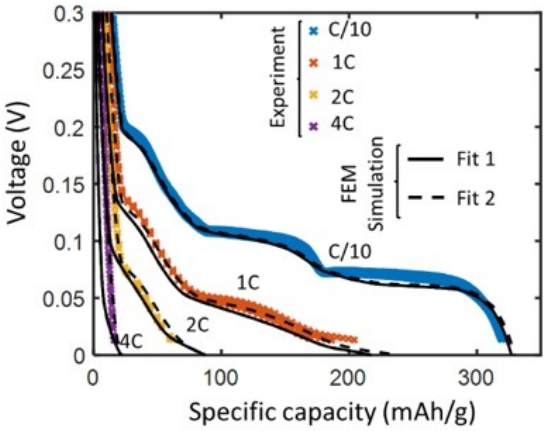

Figure S.1: Voltage fit of two p2D numerical simulations of fast-charging voltage response to graphite half cell experiments. Fit 1 has an order of magnitude lower exchange current density (of the graphite lithiation reaction) than Fit 2. By adjusting the Butler-Volmer model on the lithium metal surface, both fits show excellent agreement with experiment, even though they exhibit different substantially different plating predictions and plating mechanism. The modeling result summarized here are taken from Mijailovic et al. 2022[3], and all parameters are described in that work.

detect very small concentrations of a phase near the beginning or the end of a phase transition. This is exacerbated by the inability to identify via color alone where a certain particle lies in the narrow solid solution regime of a pure phase. However, longer wavelength deviations are also present, increasing in magnitude towards the end of the charge, and at higher rates.

Similar comparisons of the charge half cycles alone are reported in Figure S.6.The imaged SOC tends to repeatedly outpace the actual SOC towards the end of the charge, especially at high rates, where the gold LiC_6 phase fully saturates the electrode before the electrochemical capacity is exhausted. Throughout this study, we have assumed that the visible color on the surface of the particles is representative of the bulk. Our simulations using a representative solid diffusivity of $1.45 \times 10^{-13} m^2 s^{-1}$ predict very little difference between the lithium concentration of the particle surface and of the bulk, however the diffusivity is known to drop dramatically in the more lithiated stages of graphite[1,2]. The development of intra-particle gradients could explain the observed early saturation of the gold phase before the particles are fully lithiated, particularly in 50 micron samples at high rates, where the applied local current densities are the largest.

Finally, in the extreme rate experiments, the imaged SOC actually trails the electrochemically measured value. This is likely a result of lithium plating diverting current. Outside of the three extreme rate experiments, we have reasonable agreement between the electrochemical and image-derived SOC.

The same in-plane heterogeneity phenomenon is much more apparent in the ex situ cross sections Figs. S.12,S.13. In particular, the intercalation fronts consistently proceed further around the perimeter of the electrode disc than in the center, possibly due to additional intercalation via the free edges. Interestingly, plating also consistently initiates around the perimeter, a pattern consistent with the observation that plating also begins preferentially around channels. Another explanation may be the uneven stack pressure applied by the flexible stainles steel casings of the coin cells. This is supported by the fact that this effect was drastically reduced by the inclusion of more rigid spacers on either side of the electrode stack within the coin cell.

As mentioned before, the intercalation profiles presented in the main text represent only the areas boxed in blue in Figs. S.12, S.13. To quantify the error introduced, the same analysis in conducted for the entire electrode diameter (Fig. S.9). In-plane heterogeneity results in smoothing of the SOC profile and the loss of defined staging plateaus when the data is averaged in the in-plane direction. While the profile shape differs between the blue box and the whole, the aggregate image-derived SOC is very consistent, remaining within a few percent difference (Figs. S.2, S.3).

Another source of error common to both in situ and ex situ experiments is the limitations inherent to deriving SOC information from stage colors. The graphite intercalation compounds formed en route

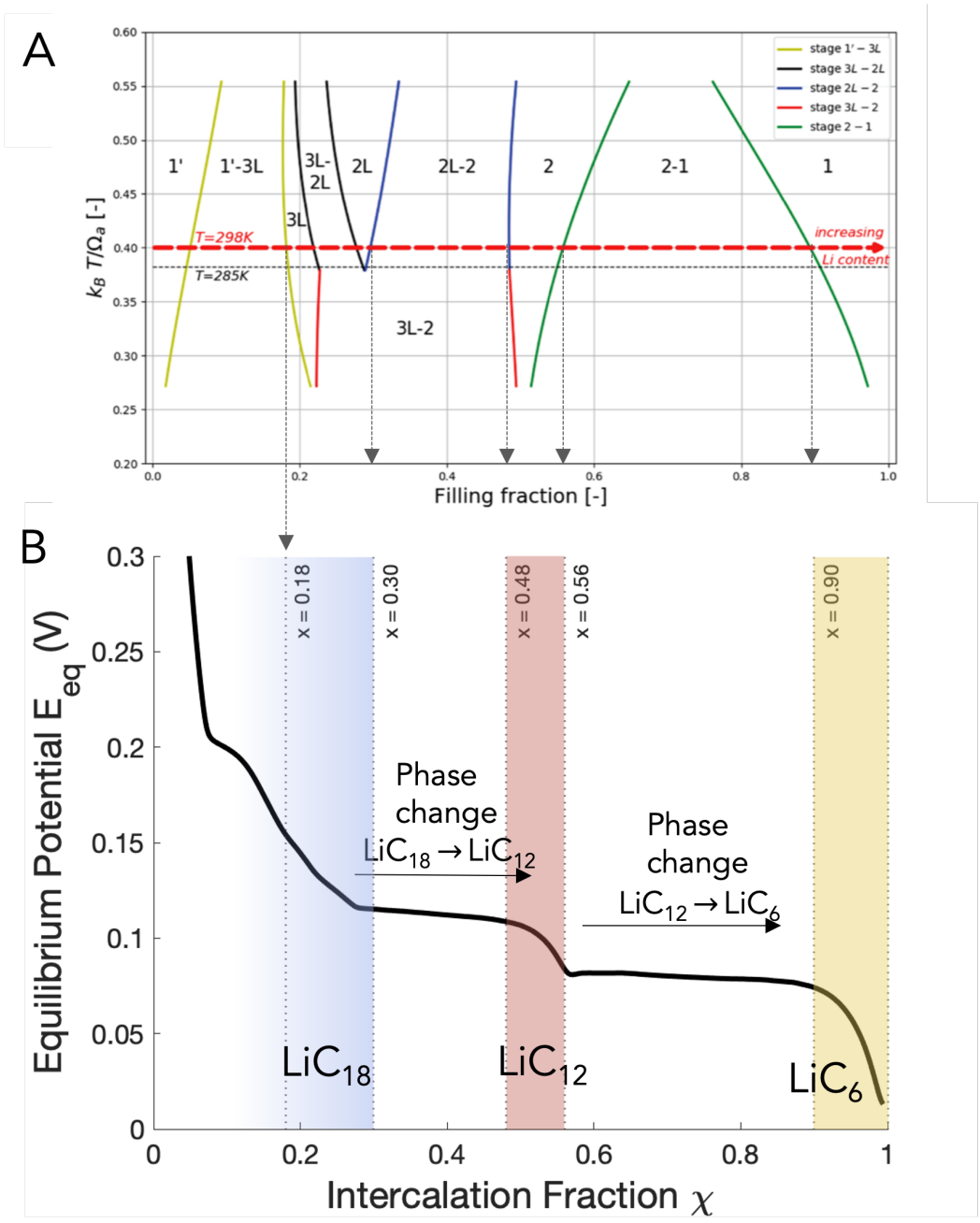

Figure S.2: A) Phase diagram of graphite intercalation compounds reproduced with permission from Rykner and Chandesris (2022)[4] showing the solid solution regions for the pure phases imaged in experiments. B) Characteristic potential curve of graphite material, obtained during a quasi-equilibrium cycle (C/40) of a 50μm electrode. Arrows from the phase diagram to the equilibrium potential indicate the assumed particle surface intercalation fractions corresponding to colors observed in imaging experiments.

Table S.1: Experimental conditions and calculated reaction inhomogeneity parameter for each in situ cell experiment.

Sample	Nominal thickness	Average post-mortem thickness	Nominal C-rate	Actual C-rate	Porosity	Calculated tortuosity	λ
CS13	150	160	C/20	0.045	0.373	4.39	0.086
CS14	150	160	C/20	0.045	0.373	4.39	0.086
CS15	100	111	C/10	0.09	0.363	4.57	0.09
CS15	100	111	C/2	0.47	0.363	4.57	0.47
CS16	100	111	1C	0.91	0.363	4.57	0.909
CS17	150	160	C/5	0.18	0.373	4.39	0.344
CS17	150	160	C/2	0.46	0.373	4.39	0.878
CS18	100	111	C/2	0.46	0.363	4.57	0.46
CS18	100	111	2C	1.96	0.363	4.57	1.958
CS20	100	111	C/10	0.089	0.363	4.57	0.089
CS23	50	66	2C	1.96	0.435	3.49	0.391
CS23	50	66	4C	4.1	0.435	3.49	0.817
CS24	50	66	0.4C	0.34	0.435	3.49	0.068
CS24	50	66	4C	3.59	0.435	3.49	0.715
CS24	50	66	8C	7.56	0.435	3.49	1.507
CS31	50	66	4C	4.06	0.435	3.49	0.809
CS33	100	111	C/10	0.11	0.363	4.57	0.11
CS38	100	111	C/10	0.1056	0.363	4.57	0.106
CS39	100	111	C/10	0.102	0.363	4.57	0.102
CS40	100	111	C/10	0.11	0.363	4.57	0.11
CS40	100	111	1C	1.03	0.363	4.57	1.029
CS44	150	160	C/10	0.1	0.373	4.39	0.191
CS44	150	160	C/5	0.2	0.373	4.39	0.382
CS45	150	160	C/2	0.55	0.373	4.39	1.05
CS46	150	160	C/2	0.54	0.373	4.39	1.031
CS56	50	66	4C	0.375	0.435	3.49	0.075
CS61	50	66	4C	3.59	0.435	3.49	0.715
CS61	50	66	2C	1.85	0.435	3.49	0.369
CS62	150	160	C/2	0.49	0.373	4.39	0.935
CS62	150	160	1C	0.99	0.373	4.39	1.89

Sample number	Dry Thickness (μm)	Plated	Target SOC (%)	Local Imaged SOC	Global Imaged SOC
32	110.5	N	40	43.2	40.9
34	100.3	N	50	47.0	47.1
35	100.3	N	40	43.3	41.6
39	102.9	N	60	59.3	57.5
40	101.6	Y	70	72.9	71.4
46	106.1	Y	80	81.1	74.8
47	102.9	Y	60	61.4	61.6
49	102.1	Y	70	73.6	69.0
57	104.6	N	50	51.2	50.6

Table S.2: Summary of all post mortem analysis of "ex situ" experiments of 102 μm cell charged at 1C. Plating is indicated, and the SOC_{app} is calculated for local imaging frame (Local Imaged SOC) and entire composite electrode (Global Imaged SOC).

Sample number	Dry Thickness (μm)	Plated	Target SOC (%)	Local Imaged SOC	Global Imaged SOC
33	54.6	Y	60	60.6	54
43	54.6	N	60	59.6	57.6
45	55.1	Y	70	68.7	65.8
50	53.3	N	40	40.6	43.4
52	54.6	N	50	51.5	48.8
53	55.3	N	40	41.1	42.0
54	53.8	Y	70	70.6	69.6
55	53.3	N	50	52.9	52.6
56	54.6	Y	80	81.6	81.9

Table S.3: Summary of all post motem analysis of "ex situ" experiments of 54 μm cell charged at 4C. Plating is indicated, and the SOC_{app} is calculated for local imaging frame (Local Imaged SOC) and entire composite electrode (Global Imaged SOC).

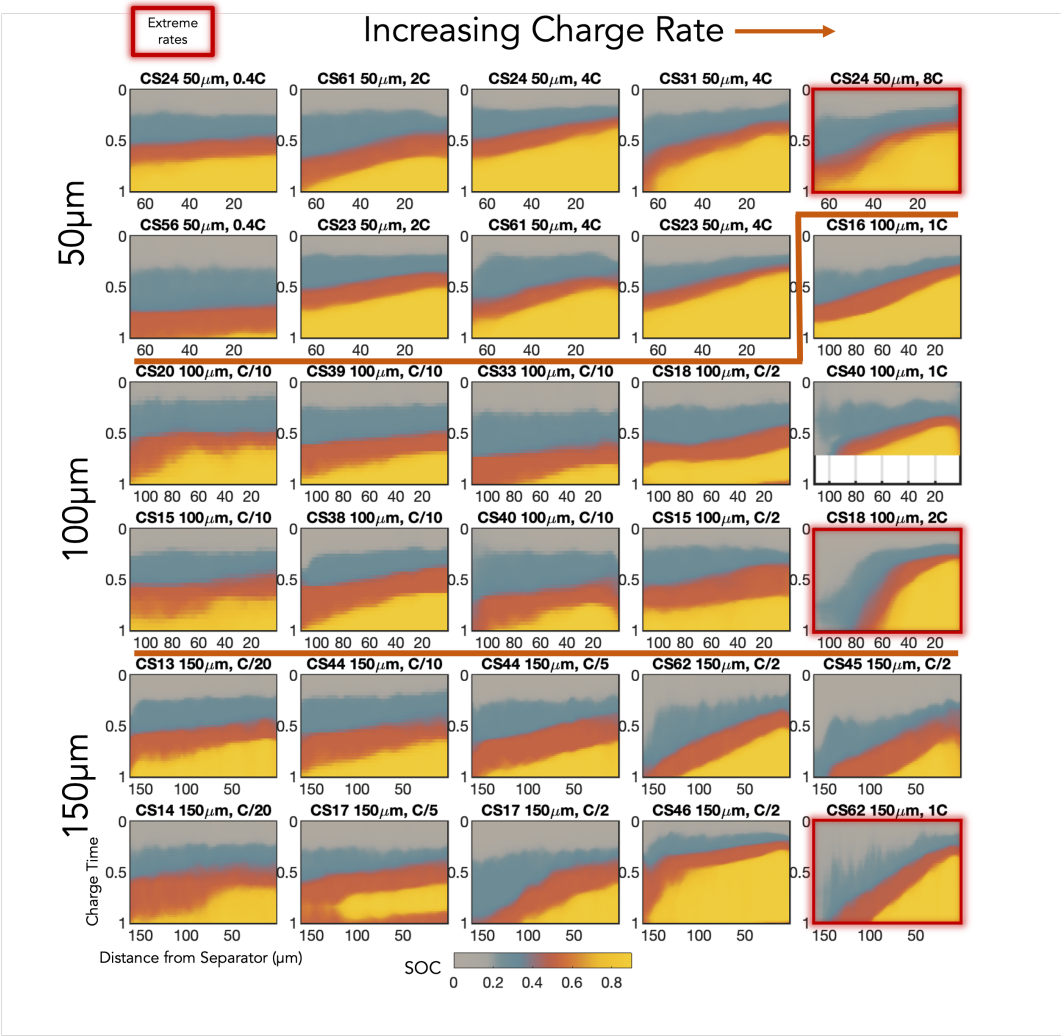

Figure S.3: Composite images showing the state of charge as a function of depth in the electrode and charge time for all in situ charge cycles. Extreme rates are highlighted in red.

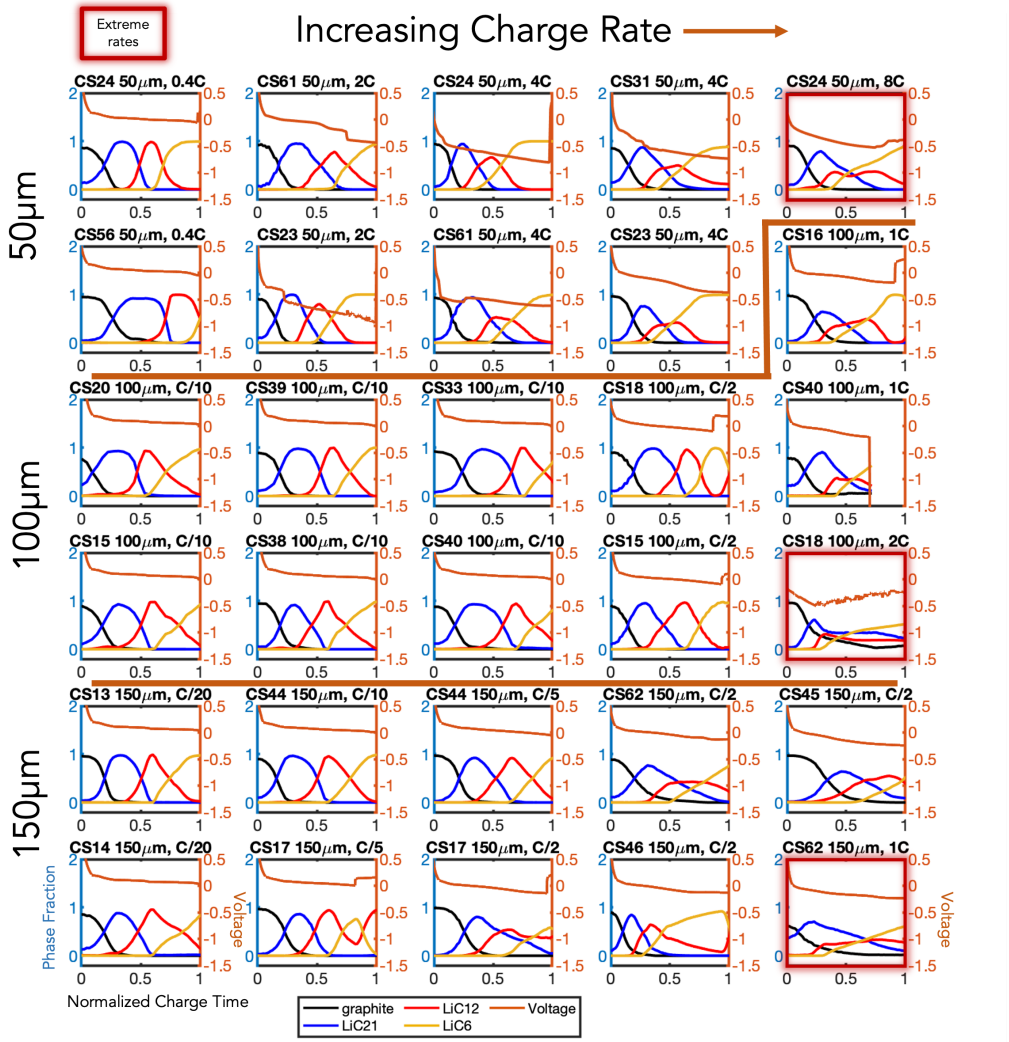

Figure S.4: Voltage response and phase fractions for all in situ charge cycles. Extreme rates are highlighted in red.

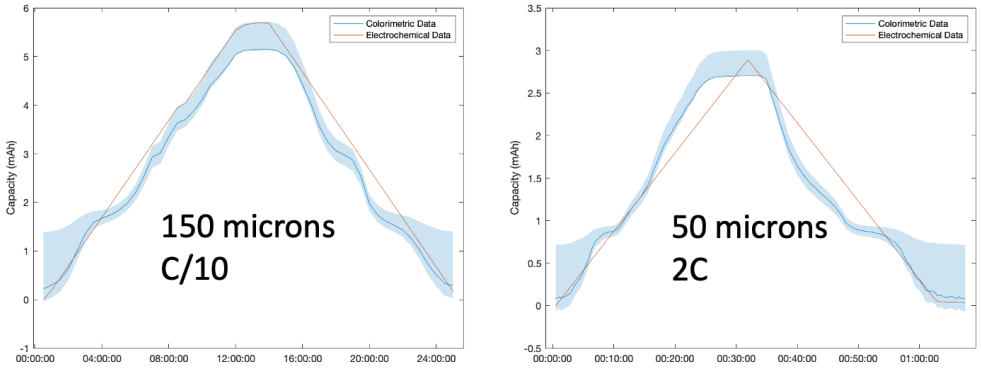

Figure S.5: Comparisons between image-derived SOC and electrochemical SOC recorded by the potentiostat for a slow charge of a 150μm thick electrode and a fast charge of a 50μm thick electrode showing the increased incongruity for higher rates and thinner electrodes

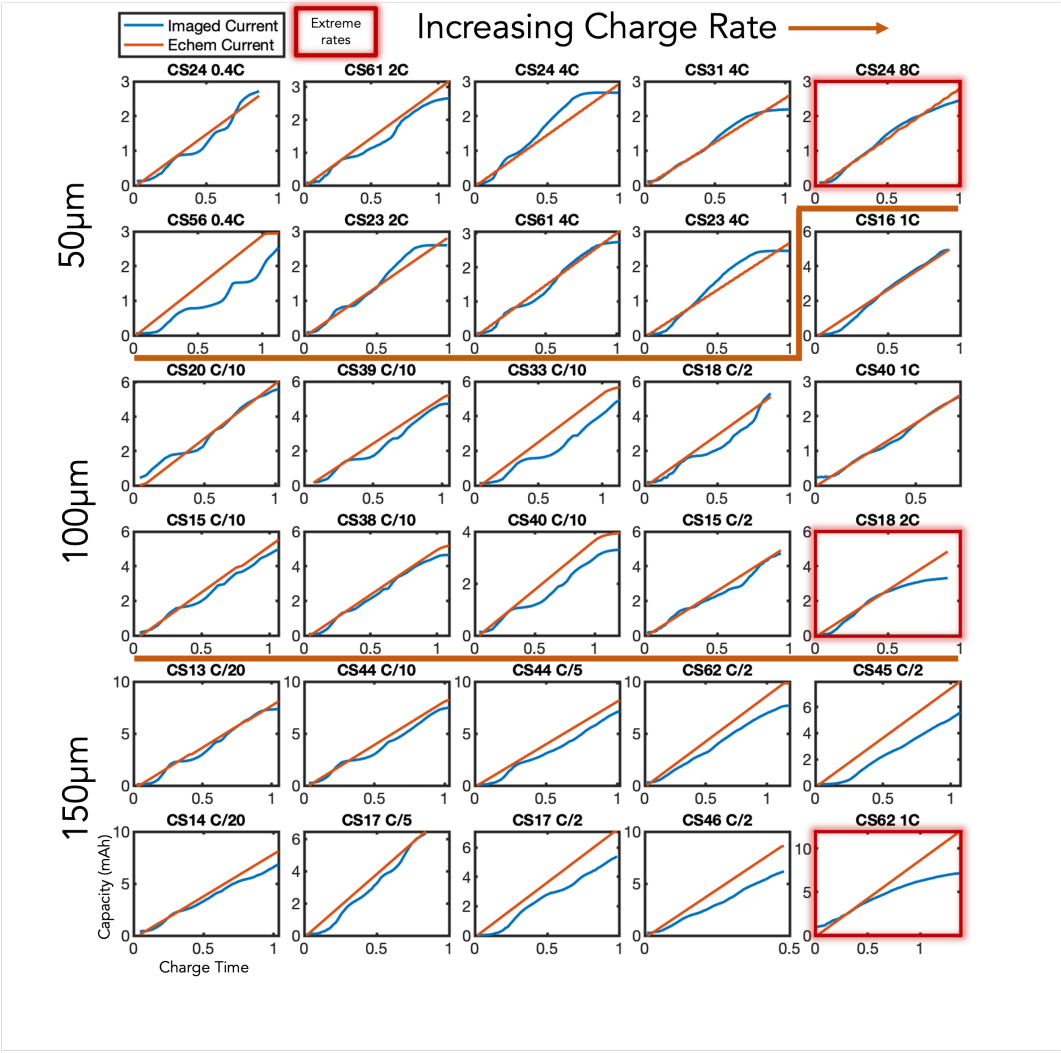

Figure S.6: Comparisons between image-derived SOC and electrochemical SOC recorded by the potentiostat for charge half cycles of all in situ experiments

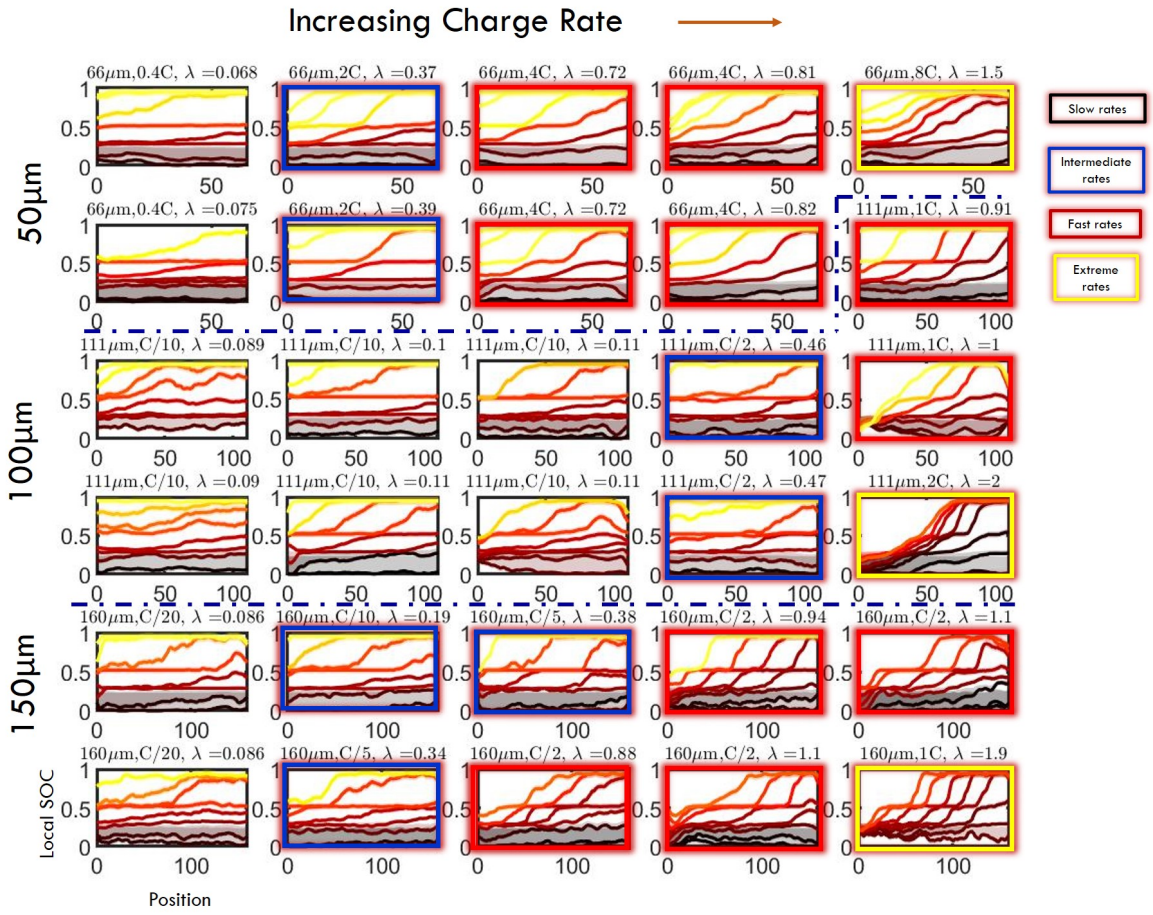

Figure S.7: Plots of SOC vs depth in the electrode at representative points during the charge cycle of all in situ electrodes. This presents the same information as Figure S.3 in a form more easily comparable to modelling results. Rates from low to extreme are highlighted with box colors.

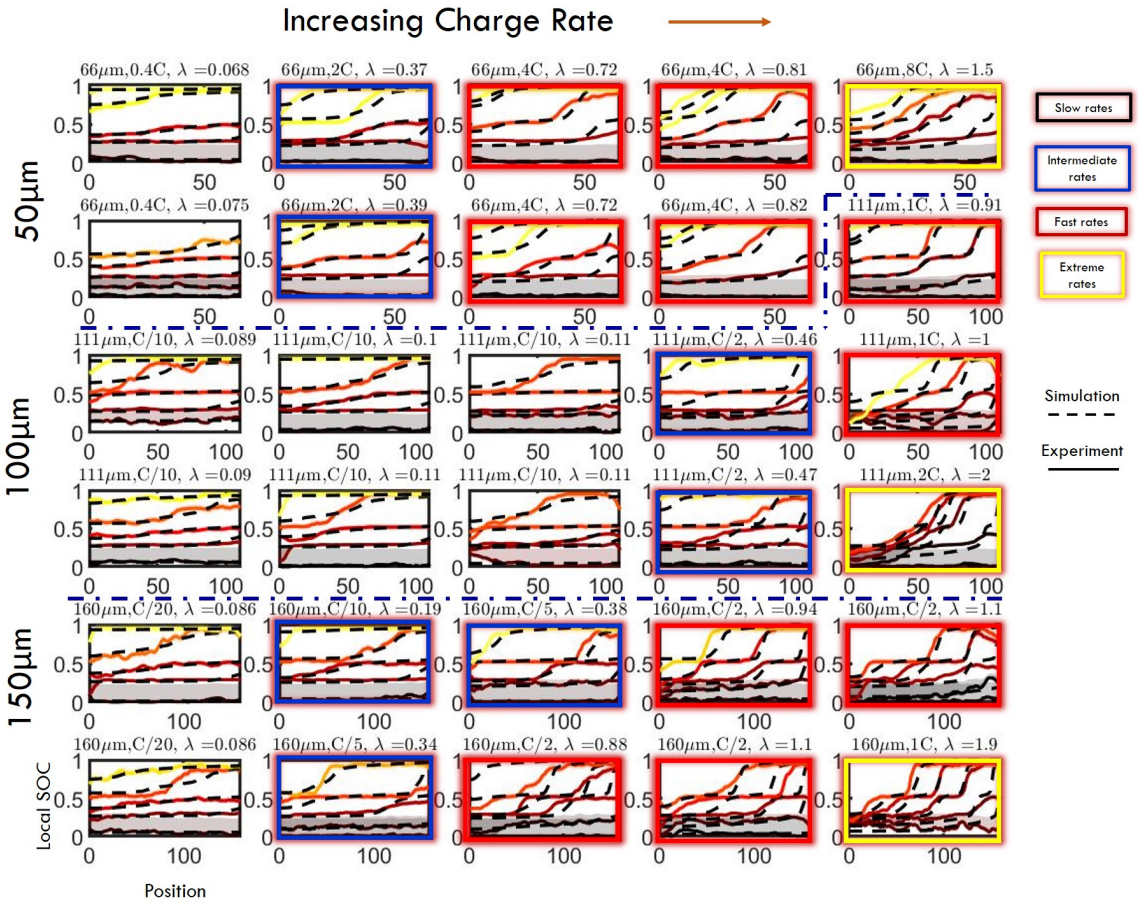

Figure S.8: Plots of SOC vs depth in the electrode at representative points during the charge cycle of all in situ electrodes (solid lines) and corresponding simulations with the p2D finite element model (dashed lines). This presents the same information as Figure S.7 but with fewer traces for easy comparison to simulations. Rates from low to extreme are highlighted with box colors.

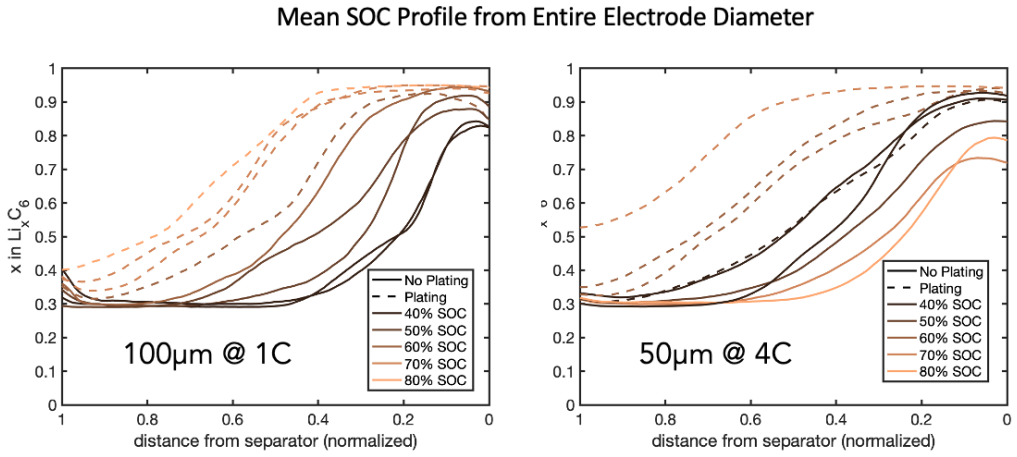

Figure S.9: SOC profiles of both ex situ series of experiments. Here the entire visible width (i.e. the 14mm diameter) of the electrode is analyzed. These are analogous to the plots presented in 7 where only the areas boxed in blue in S.12 and S.13 are presented.

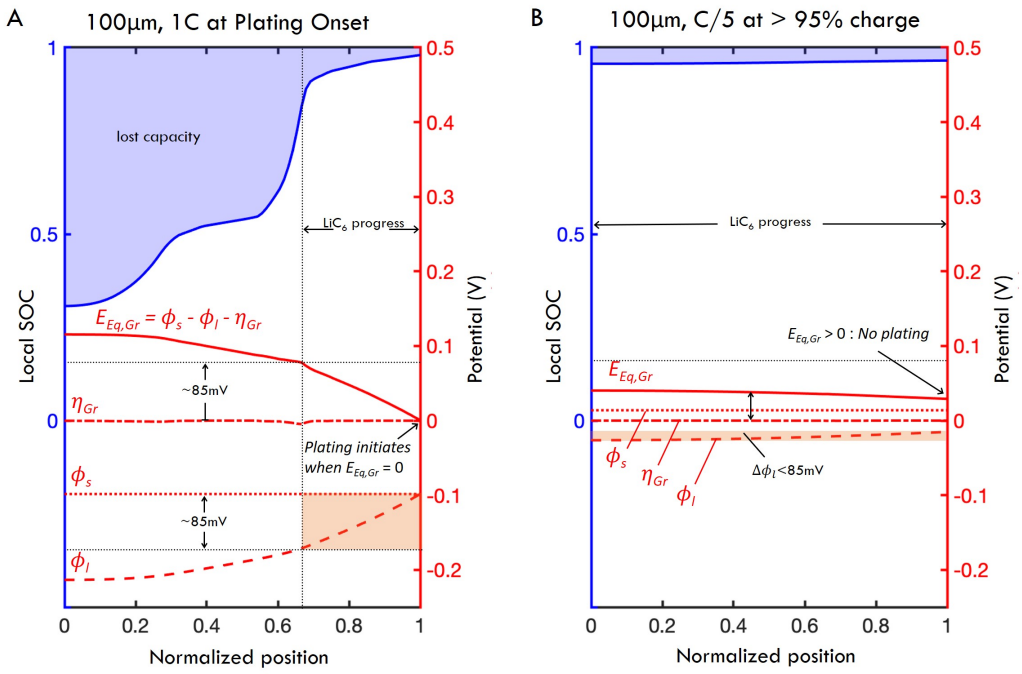

Figure S.10: Comparison of potential landscape at plating onset between A) 100μm thick cell charged at 1C vs B) at C/5. When charged at C/5, the cell has minimal capacity loss (i.e., will not plate at >95% charge) because of low polarization in E_{eq} and ϕ_l.

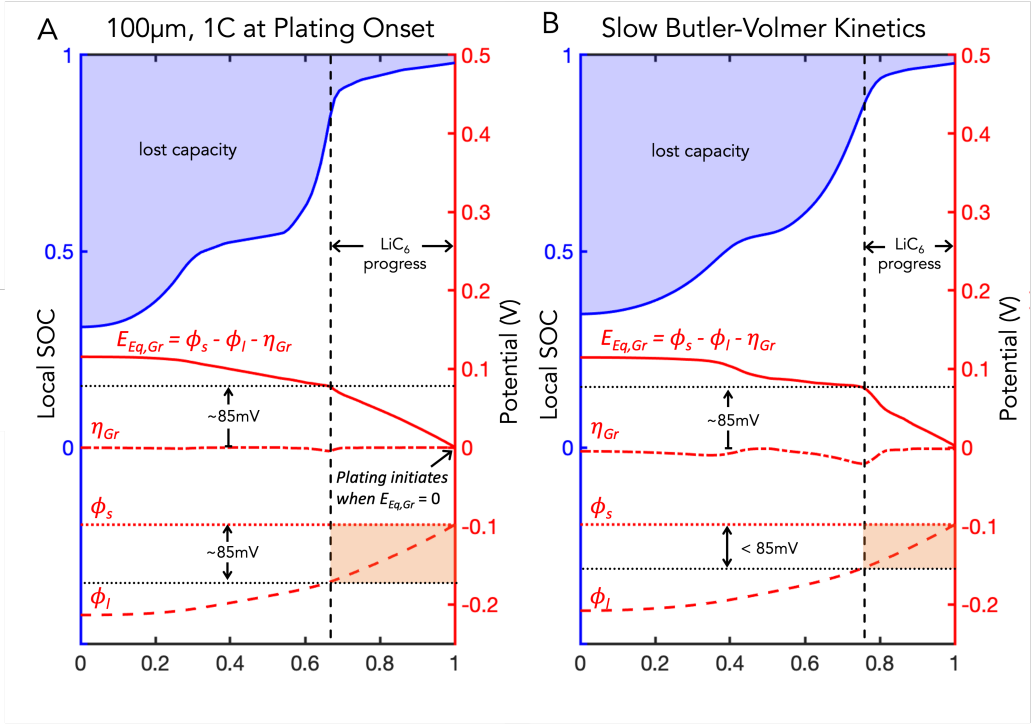

Figure S.11: Comparison of potential landscape at plating onset between A) model as implemented and B) model with slow Butler-Volmer charge transfer kinetics.

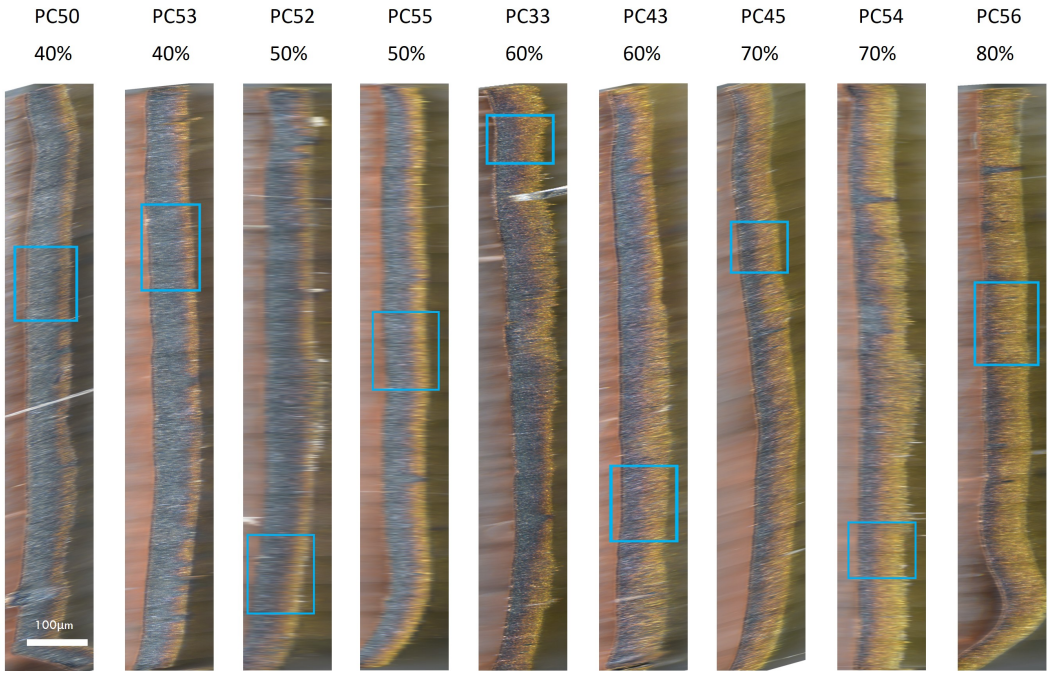

Figure S.12: Composite images of full 14mm diameter of all 50 μm samples, stitched together from many smaller images and stretched horizontally for clarity. Blue boxes indicate areas analyzed in Figure 7. Various degrees of in-plane heterogeneity are evident

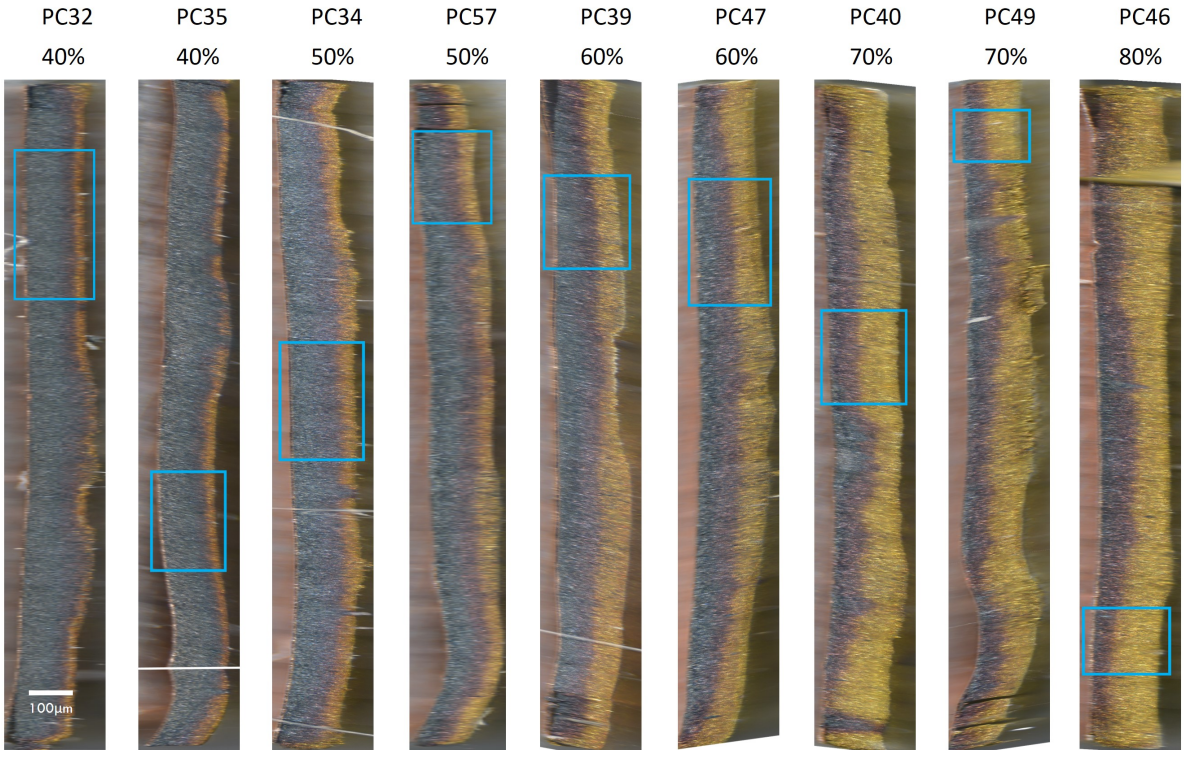

Figure S.13: Composite images of full 14mm diameter of all 100 μm samples, stitched together from many smaller images and stretched horizontally for clarity. Blue boxes indicate areas analyzed in Figure 7. White streaks are fiber contaminants from the disassembly and rinsing process

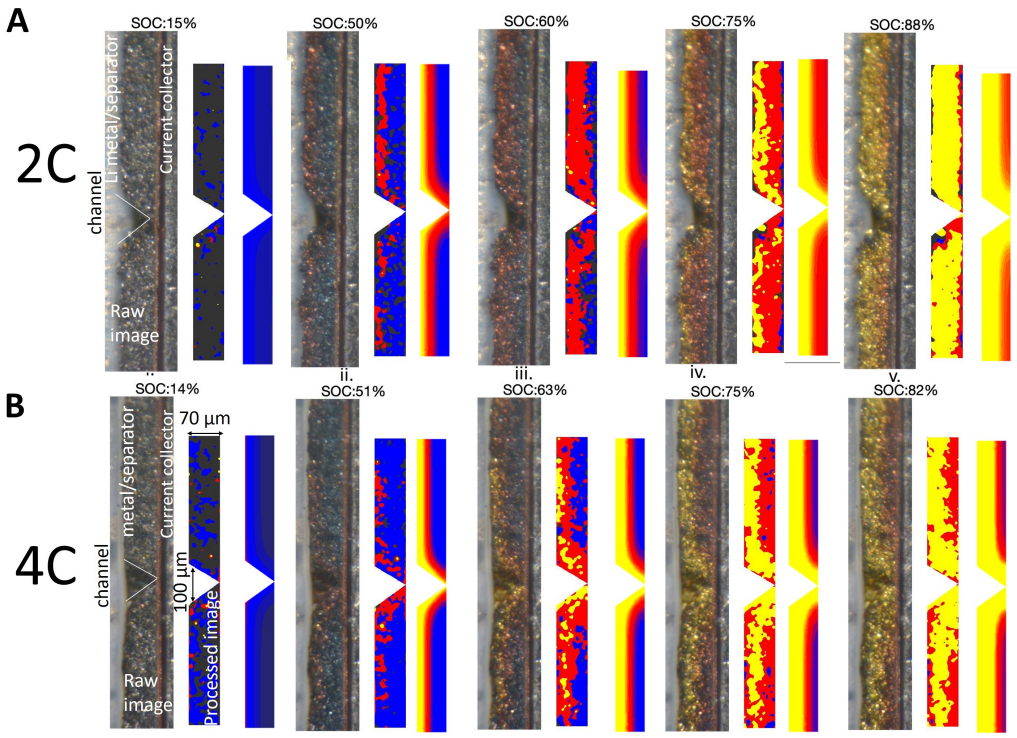

Figure S.14: Imaging and simulation of a two electrode samples with electrolyte filled channels charged at A) 2C and B) 4C.

to fully-lithiated graphite are distinct thermodynamic phases. The structures of each determine their maximum lithium capacity Fig. 3 A) as well as their evident color, via shifting the Drude edge of the reflectance spectrum to higher frequency for more lithiated stages. While Stage 1 (LiC_6, gold) and Stage 2 (LiC_{12}, red) are well characterized,[5,6] there is less consensus on the blue phase, which is commonly identified as 'dilute Stage 2' or Stage 2L[7–9] and which displays little long-range order. There may be several compounds that appear blue. There are even reports of hysteresis in staging[10], as well evidence that many of the structures access are purely metastable[11]. We thus elect to use the stoichiometry reported in the phase diagram constructed by Rykner and Chandesris, reproduced in Figure S.2. They determined via thorough phase-field modelling, which takes into account inter- and intra-layer interactions of intercalated ions to describe the phase separation behavior observed[4]. Likely, several dilute stages have been lumped together empirically under the blue Stage 2L category based on the corroboration between the color response and electrochemical data, a choice supported by the staging hysteresis reported in the literature.

Beyond the uncertainty in the dilute stages, neither Stage 2 nor Stage 1 are line compounds, each with a small solid solution region surrounding their nominal stoichiometry S.2. The inability to distinguish particles occupying these regions leads to inherent uncertainty in our SOC calculation, which is represented by the shaded confidence intervals in the SOC plots. Using a single target color for each phase, it is not possible, therefore, to distinguish between a particle at 90% SOC and one that is fully lithiated. This in addition to the inability of our optics to resolve small regions in a particle occupying different stages results in slight step structure of figures S.5 and S.6.

S.2 Phase Separation

To improve upon the p2D model, other porous electrode theory formulations, such as phase-field modeling have been developed to better model such phase-separating materials. It is postulated that the agreement between the p2D model and experimental results here may be due to the choice of small particle size for two reasons. First, the small particle size of the graphite allows for much faster intercalation within particles, which allows the assumption of roughly uniform particle intercalation at timescales relevant to charging. Second, the large number of particles makes the assumption of a "continuum" model more accurate. This last point is interesting mechanistically as individual particles do not intercalate with "solid solution" type behavior, and rather change phases abruptly while other neighboring particles have not changed phase. This results in the "mosaic" pattern observed in colorimetry of graphite electrodes. This phenomenon was reproduced here by interrupting a fast charging cycle with a prolonged OCV period, during which the mosaic pattern became much more apparent due to relaxation of intercalation gradients (Fig. S.18). However, it is hypothesized here that, given a sufficient number particles, it may be assumed that a large enough volume of the electrode may on average behave like a solid solution, even though individual particles do not. Indeed, in the aforementioned experiment, the timescale upon which the mosaic pattern evolved to dominate the overall intercalation gradient was an order of magnitude longer than that of the fast charge cycle (Fig. S.18). The result is that reaction fronts through the electrode through-thickness change slope as the C-rate varies, as predicted by the p2D model (see Figs. 5 and 7). However, when particles are large with respect to the electrode thickness (as may begin to occur in the 50 μm cell in Fig. 7) the slopes of the staging plateaus may not match the model as well due to breakdown of continuum models (including p2D and other PET formulations).

To examine the extent of relaxation in intercalation gradients, a $100\mu m$ sample was cycled at C/10 and abruptly put under an open circuit rest condition in the middle of the Stage 1-Stage 2 transition during discharge. At the beginning of the experiment, a mild gradient is visible. Over the course of the OCV rest period, the gradient relaxes, with the final image showing a uniform SOC across the width of the electrode (Fig. S.18 D). The cumulative fractions of Stage 1 (gold) imaged anywhere on the electrode surface declines linearly with time (Fig. S.18 B), indicating there may be some self-discharge mechanism at play. However the final image during the OCV period reveals an accentuated "mosaic" pattern, with isolated particles that remain fully gold in contrast with their neighbors. This may be evidence of phase separation, where some particles fully transform to Stage 1 at the expense of others which discharge to Stage 2 in order to lower the energy penalty associated with phase boundaries[13]. The particles that remained gold promptly changed color along with the rest of the electrode once cycling was resumed, indicating there was no loss of electrical contact.

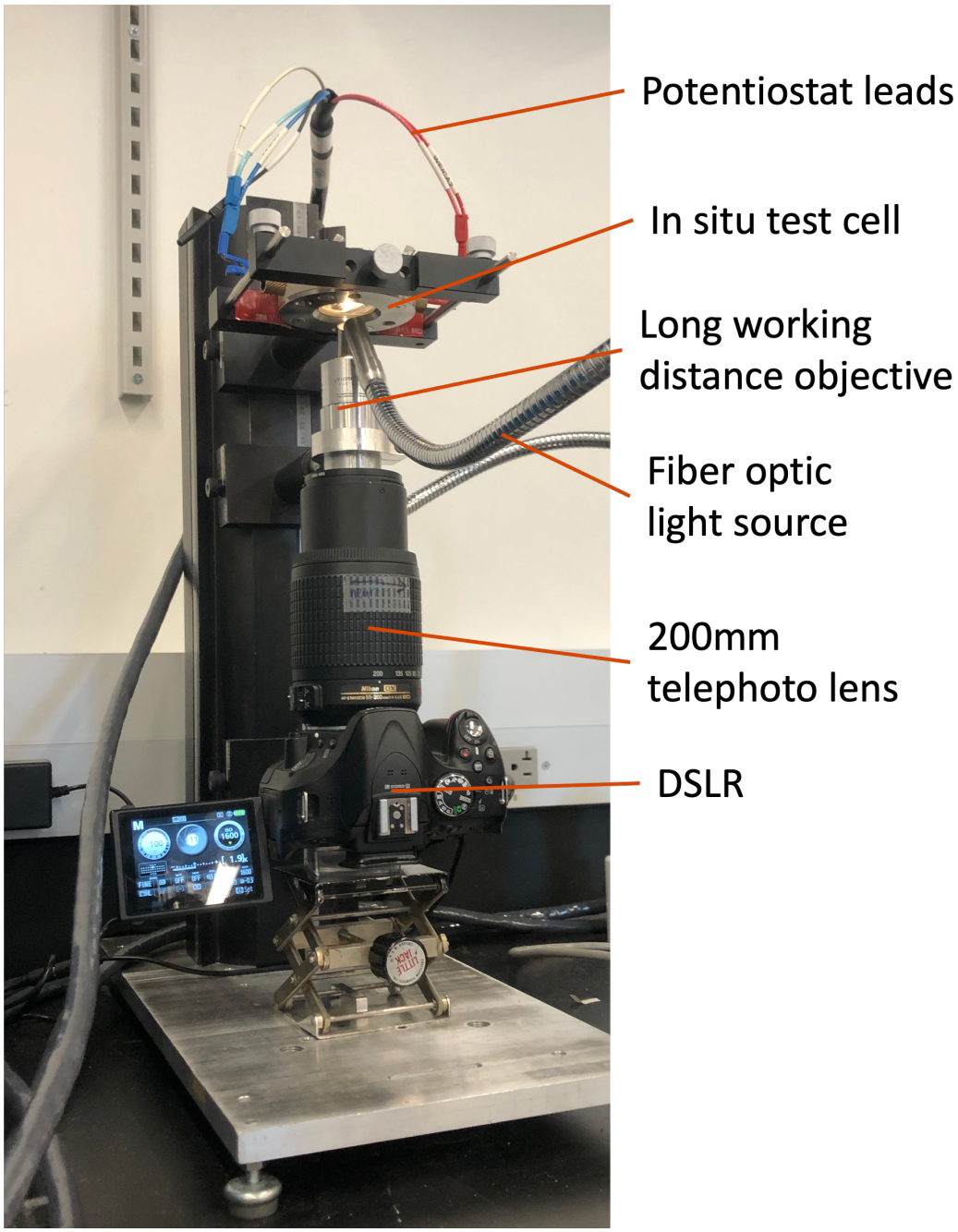

Figure S.15: Imaging equipment consisting of a long-working-distance microscope objective mounted to a consumer-grade DSLR with an intervalometer via a filter adapter and a 200mm telephoto lens. All optical components were mounted to a rigid optical rail and a delayed shutter was used to minimize vibrations. The entire test cell and imaging assembly was inverted to ensure the electrode remained submerged as well as evacuation of any bubbles evolved in the electrode during SEI formation

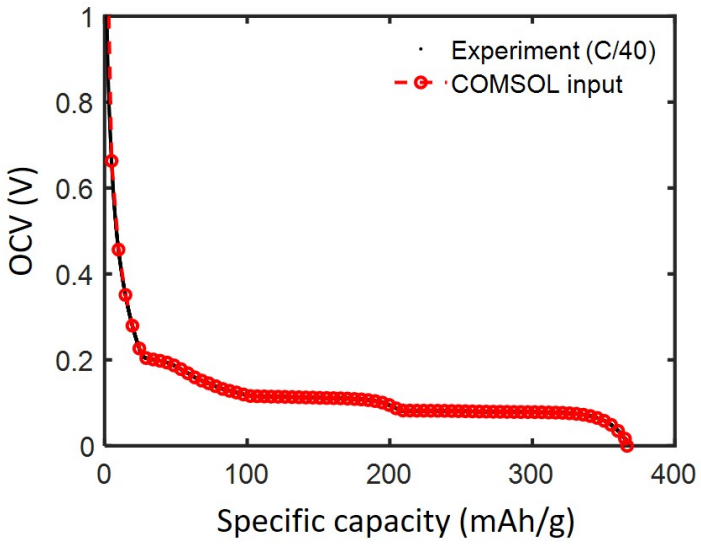

Figure S.16: Graphite voltage during C/40 charge (open circuit voltage) vs specific capacity and input data for graphite equilibrium potential in the finite element model. Points are used as input in COMSOL with spline interpolation.

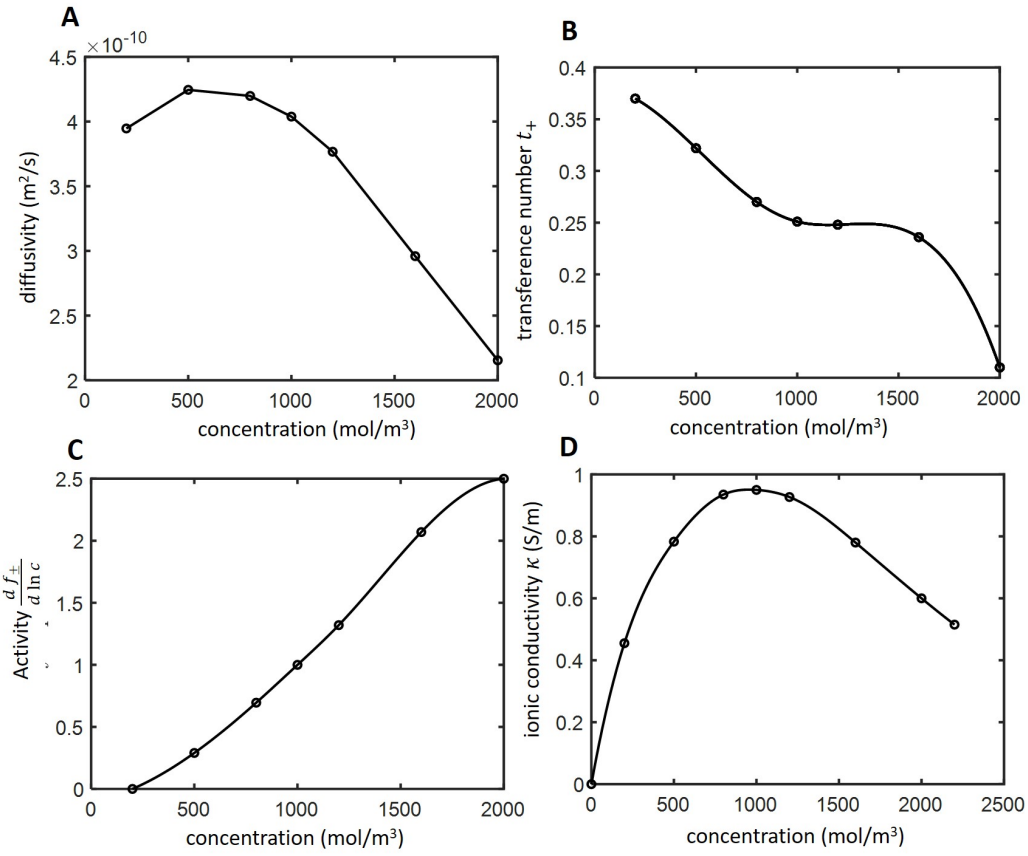

Figure S.17: Material properties used in graphite anode in half-cell simulations. (A) Diffusivity D , (B) transference number t_+ , (C) activity coefficient[12], (D) ionic conductivity κ as a function of Li^+ concentration c. Points are used as input in COMSOL with spline interpolation. Extrapolating beyond the concentrations depicted here, properties are assumed constant.

Table S.4: Anode properties for numerical model.

	Symbol	Graphite
Porosity	ϵ_e	as indicated
Active solid fraction	ϵ_s	$(1-\epsilon_e)\times 0.94$
Particle diameter (µm)	a	6.5 †
Active specific surface area (1/m)	a_c	4.6×10^6
Tortuosity (through plane)	τ	$\epsilon_e^{-1.5}$ (emperical fit)
Equilibrium potential (V)	E_{eq}	Fig. S.16A
Slope of equilibrium potential (V)	K	$\frac{dE_{eq}(\chi)}{d\chi}$
Electrical conductivity (S/m)	σ	100
Effective electrical conductivity (S/m)	σ_{eff}	100
Solid phase Li^+ diffusivity (m^2/s)	D_s	1.45×10^{-13}
Theoretical maximum concentration of Li in anode (mol/m^3)	c^{o}	31920
Effective maximum concentration of Li in anode (mol/m^3)	c_{max}	29047
Initial intercalation fraction		0.001
Maximum intercalation fraction		1
Exchange current density, Butler-Volmer (A/m^2)	i_0	$Fk_0c^{1-\alpha_c}c_s^{\alpha_a}(c^{\text{o}}-c_s)^{\alpha_a}$
Reaction rate constant $(\frac{\text{mol}}{\text{m}^2\text{s}}(\frac{\text{mol}}{\text{m}^3})^{-1.5})$	k_0	1×10^{-10} (exept 1×10^{-11} when "slow" is indicated)
Anodic transfer coefficient	α_a	0.5
Cathodic transfer coefficient	α_c	0.5

References

1. Persson K, Sethuraman VA, Hardwick LJ, Hinuma Y, Meng YS, Ven A van der, Srinivasan V, Kostecki R, and Ceder G. Lithium Diffusion in Graphitic Carbon. The Journal of Physical Chemistry Letters 2010; 1. Publisher: American Chemical Society:1176–80
2. Heß M and Novák P. Shrinking annuli mechanism and stage-dependent rate capability of thin-layer graphite electrodes for lithium-ion batteries. Electrochimica Acta 2013; 106:149–58. DOI: 10.1016/j.electacta.2013.05.056
3. Mijailovic AS, Wang G, Li Y, Yang J, Lu W, Wu Q, and Sheldon BW. Analytical and numerical analysis of lithium plating onset in single and bilayer graphite electrodes during fast charging. Journal of The Electrochemical Society 2022; 169:060529. DOI: 10.1149/1945-7111/ac73bb
4. Rykner M and Chandesris M. Free Energy Model for Lithium Intercalation in Graphite: Focusing on the Coupling with Graphene Stacking Sequence. The Journal of Physical Chemistry C 2022; 126:5457–72. DOI: 10.1021/acs.jpcc.1c10800
5. Woo KC, Mertwoy H, Fischer JE, Kamitakahara WA, and Robinson DS. Experimental phase diagram of lithium-intercalated graphite. Physical Review B 1983; 27:7831–4. DOI: 10.1103/PhysRevB.27.7831
6. Dahn JR. Phase diagram of Li_xC_6. Physical Review B 1991; 44. Publisher: American Physical Society:9170–7. DOI: 10.1103/PhysRevB.44.9170

Table S.5: Electrolyte properties ($LiPF_6$ in 3:7 EC:EMC).

	Symbol	Electrolyte
Initial salt concentration (mol/m^3)	c_0	1200
Ionic conductivity (S/m)	κ	Fig. S.17D
Li^+ Diffusivity (m^2/s)	D	Fig. S.17E
Effective ionic conductivity (S/m)	κ_{eff}	$\kappa \times \frac{\epsilon_e}{\tau}$
Effective diffusivity m^2/s	D_{eff}	$D \times \frac{\epsilon_e}{\tau}$
Activity coefficient	$\frac{d\ln f_{\pm}}{d\ln c}$	Fig. S.17C
Transference number	t_+	Fig. S.17B

Table S.6: Separator properties.

	Separator
Thickness (µm)	25
Porosity	40%
Tortuosity	$\epsilon_e^{-0.5}$

Table S.7: Li metal electrode properties.

	Graphite
Exchange current density (A/m^2)	8.5
Anodic transfer coefficient	0.5
Cathodic transfer coefficient	0.5
Electrolyte reference concentration (mol/m^3)	1200
Equilibrium potential (V)	0

Table S.8: Parameters for scaling law

variable	value
$c_{\max}$	29000
t^+	0.25
$\frac{\partial f_{\mp}}{\partial \ln c}$	1.3
c_0	1200 mol/m^3
U	0.2 V
κ	0.9 S/m
κ_{eff}	$\kappa \times \frac{\tau_Z}{\epsilon_e}$
D	3.5 $\times 10^{-10}$ m^2/s
D_{eff}	$D \times \frac{\tau_Z}{\epsilon_e}$
$\mathcal{T}_0$	298 K

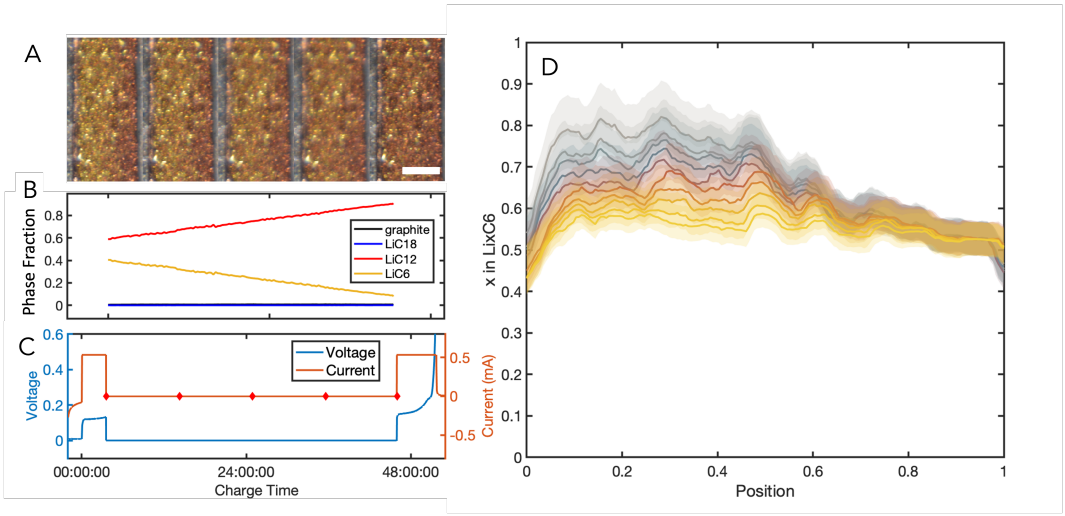

Figure S.18: A) Selected images of high rate relaxation experiment. Scale bar is 100 μm B) Processed cumulative phase fractions during the OCV period. C) Electrochemical data showing 40 hr OCV condition. Red diamonds indicate locations of images in A. D) SOC vs position over the course of the OCV period. Color scale indicates progression of 10 equally spaced snapshots.

7. Tran TD, Song XY, and Kinoshita K. Investigation of Lithiated Carbons by Transmission Electron Microscopy and X-Ray Diffraction Analysis. MRS Proceedings 1998; 548:37. DOI: 10.1557/PROC-548-37

8. Billaud D, Henry FX, Lelaurain M, and Willmann P. Revisited structures of dense and dilute stage II lithium-graphite intercalation compounds. Journal of Physics and Chemistry of Solids. Proceeding of the 8th International Symposium on Intercalation Compounds 1996; 57:775–81. DOI: 10.1016/0022-3697(95)00348-7

9. Ohzuku T, Iwakoshi Y, and Sawai K. Formation of Lithium-Graphite Intercalation Compounds in Nonaqueous Electrolytes and Their Application as a Negative Electrode for a Lithium Ion (Shuttlecock) Cell. Journal of The Electrochemical Society 1993; 140. Publisher: IOP Publishing:2490. DOI: 10.1149/1.2220849

10. Mercer MP, Peng C, Soares C, Hoster HE, and Kramer D. Voltage hysteresis during lithiation/delithiation of graphite associated with meta-stable carbon stackings. Journal of Materials Chemistry A 2021; 9:492–504. DOI: 10.1039/D0TA10403E

11. Gavilán-Arriazu EM, Pinto OA, López de Mishima BA, Barraco DE, Oviedo OA, and Leiva EPM. The kinetic origin of the Daumas-Hérold model for the Li-ion/graphite intercalation system. Electrochemistry Communications 2018; 93:133–7. DOI: 10.1016/j.elecom.2018.07.004

12. Nyman A, Behm M, and Lindbergh G. Electrochemical characterisation and modelling of the mass transport phenomena in LiPF6–EC–EMC electrolyte. Electrochim. Acta 2008; 53:6356–65

13. Ferguson TR and Bazant MZ. Nonequilibrium thermodynamics of porous electrodes. Journal of The Electrochemical Society 2012; 159:A1967. DOI: 10.1149/2.048212jes